







## Anisotropic rheology and friction of suspended graphene

Andrea Mescola <sup>1</sup>, Andrea Silva <sup>2,3</sup>, Ali Khosravi <sup>2,3,4</sup>, Andrea Vanossi <sup>2,3</sup>, Erio Tosatti <sup>2,3,4</sup>,  
Sergio Valeri,<sup>1,5</sup> and Guido Paolicelli <sup>1,\*</sup>

<sup>1</sup>CNR-NANO, Consiglio Nazionale delle Ricerche - Istituto Nanoscienze, Via Campi 213 41125 Modena, Italy

<sup>2</sup>CNR-IOM, Consiglio Nazionale delle Ricerche - Istituto Officina dei Materiali, c/o SISSA Via Bonomea 265, 34136 Trieste, Italy

<sup>3</sup>International School for Advanced Studies (SISSA), Via Bonomea 265, 34136 Trieste, Italy

<sup>4</sup>The Abdus Salam International Centre for Theoretical Physics (ICTP), Strada Costiera 11, 34151 Trieste, Italy

<sup>5</sup>Department of Physics, Informatics and Mathematics, University of Modena and Reggio Emilia, Via Campi 213 41125 Modena, Italy



(Received 7 February 2023; accepted 20 April 2023; published 17 May 2023)

Graphene is a powerful membrane prototype for both applications and fundamental research. Rheological phenomena including indentation, twisting, and wrinkling in deposited and suspended graphene are actively investigated to unravel the mechanical laws at the nanoscale. Most studies focused on isotropic setups, while realistic graphene membranes are often subject to strongly anisotropic constraints, with important consequences for the rheology, strain, indentation, and friction in engineering conditions. Graphene in particular is recognized as the thinnest solid lubricant material and a large amount of work has been dedicated to understanding the fundamentals mechanisms of this effect and to unravel parameters relevant to its technological development. Here, we experimentally show how graphene's frictional response to an external indenter is severely altered by conditions of anisotropic suspension, specifically when graphene is clamped across a long and narrow groove. Results show that the friction coefficient is significant when the tip is sliding parallel to the groove while becoming ultralow in the orthogonal direction. While the experimental data suggest that—rather unexpectedly—prestrain of the graphene sheet as a result of clamping is negligible, the key to understanding the underlying mechanism is provided by simulations. The paramount mechanism is provided by the extra anisotropic strain induced from indentation under anisotropic constraints, which in turn produces an anisotropic stiffening of the graphene. While the focus of this work is on graphene, we believe our experimental protocol and the physical mechanism uncovered by our model can be applicable to other 2D membranelike materials.

DOI: [10.1103/PhysRevMaterials.7.054007](https://doi.org/10.1103/PhysRevMaterials.7.054007)

### I. INTRODUCTION

The rheological and frictional behavior of pristine graphene has attracted much fundamental and technological interest during the last decade. From the mesoscale down to the atomic level, a great research effort is underway to unveil the physical mechanisms underpinning the indentation, twisting, wrinkling, and crumbling phenomena [1–8] of this extraordinary membrane. The exceptional hardness (Young's modulus around 1 TPa and intrinsic in-plane strength of 130 GPa [5]), the extreme ability to elastically sustain tensile strain up to at least 20% [9], and its large out-of-plane membranelike flexibility make graphene the forefront prototype material for the design of innovative systems and structures with controlled intrinsic properties [10]. Graphene has been integrated into several hi-tech electronic devices such as organic light-emitting diodes [11,12], strain sensors [13–17], wearable devices [18–20], and micro- and nanoelectromechanical systems [21]. Understanding and exploiting strain-induced effects in 2D layered materials in general is nowadays a fast-growing topic in both fundamental and applied research, given that many of its intrinsic properties

can be tuned by mechanical deformation. While the tunability of transport and optical properties under strain has been extensively addressed [22–26], the microscopic tribological behavior as a function of the applied strain and boundary conditions has received far less attention [27–29]. Graphene tends to conform to the morphology of the supporting surface when deposited over a hosting substrate and the tribological response of the layered coating significantly depends on the layer-substrate interaction [30–32]. At the same time, different experimental realizations of supported graphene have highlighted the importance of 2D layer strain on the overall tribological and electronic behavior [33–36]. To disentangle these effects and shed light on their origin, suspended graphene represents an ideal system. Recently, free-standing graphene has been investigated by Zhang *et al.* [27], who found a reduction of friction with increasing strain in a suspended and isotropically strained graphene sheet with atomic force microscopy (AFM) measurements. Complementary atomistic simulations showed how this tensile prestrain reduces the membrane flexibility thus decreasing the impact of the tip, hence reducing the friction.

Here we go beyond the isotropic setup in Ref. [27] and study the friction behavior of graphene suspended and fixed at the edges of a long narrow groove. We observe with remarkable reproducibility that the frictional dissipation of the

\*guido.paolicelli@nano.cnr.it

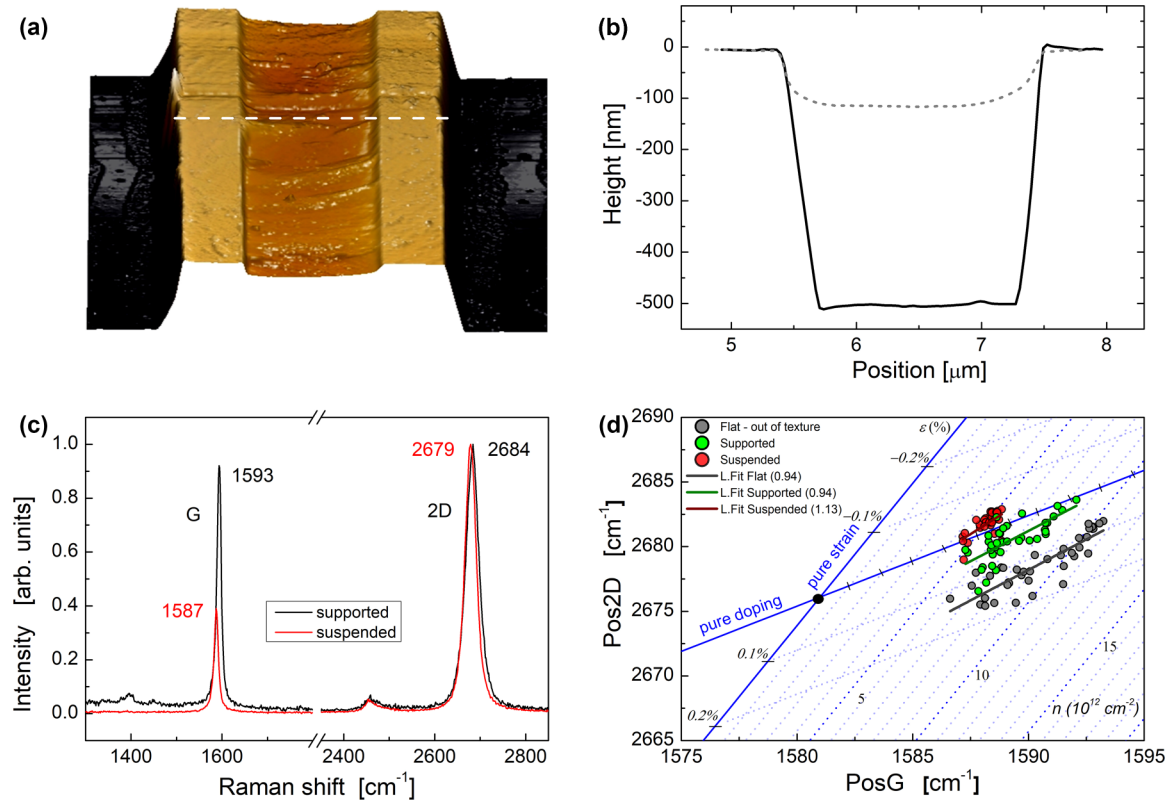


FIG. 1. AFM imaging and Raman characterization of single-layer CVD graphene anisotropically suspended. (a) Three-dimensional topography image and (b) relative line profiles of CVD graphene deposited on a single groove. White dashed line in (a) indicates the line profile in (b). Equilibrium configuration between graphene and underlying substrate indicates a complete conformation and clamping on the flat crests enclosing the groove and a total suspension at the center of the groove. (c) Raman spectra comparison of supported graphene (black) and suspended graphene (red). Note the typical redshift of  $G$  and  $2D$  peak positions on suspended graphene. (d) Correlation plot of  $\text{Pos}2D$  vs  $\text{Pos}G$  peaks showing data from supported graphene (gray) and data within the patterned area which include supported graphene on the crest and suspended graphene (green and red, respectively). Lines represent the linear fit from supported graphene (gray line, slope 0.94), graphene on crest (green line, slope 0.94), and from suspended graphene (red line, slope 1.13). Neutrality point indicated by the black dot at position ( $1581.6$  and  $2676.9 \text{ cm}^{-1}$ ) in the  $\text{Pos}2D$  versus  $\text{Pos}G$  correlation plot, and the additional axes to quantify strain and doping are taken from Ref. [36].

graphene membrane measured by our sliding AFM tip turns anisotropic, with a differential friction coefficient (COF) typically three times higher parallel to the groove axis compared to orthogonal axis. This occurs with negligible prestrain in our system, as confirmed by Raman measurements. Molecular-dynamics (MD) simulations reveal that the sliding-friction anisotropy is ruled by the interplay between the tip-indenting action and the boundary conditions. The strain-free, asymmetric suspension condition is responsible for the anisotropic indentation pattern shape and rheology of the membrane, quantitatively explaining the observations. Our results rationalize the often-overlooked aspect of nonisotropic constraints in nanoscale systems, with important implications for realistic engineering setups.

## II. SAMPLE CHARACTERIZATION

The suspended graphene was obtained by depositing a commercial single-layer chemical vapor deposition (CVD) graphene on a standard silicon dioxide-based calibration grating array.

A schematic representation of the sample construction is shown in Supplemental Material [37]. Briefly, a commercial

single-layer CVD graphene was deposited over the calibration grating by wet transfer process. The calibration grating comprises a central patterned area and a surrounding flat region. The pattern consists of long, parallel, and equally spaced grooves (crest-to-crest distance:  $3 \mu\text{m}$ , valley width:  $2 \mu\text{m}$ , step height:  $500 \text{ nm}$ ). After transfer, the external flat region is fully covered by single-layer graphene that we refer to as supported graphene in the following. On the contrary, the sample surface over patterned area displayed regions where the graphene adhered to the substrate and regions where it hung fully suspended via clamping on the top of the crests [Fig. 1(a)]. AFM 3D topography and corresponding line profiles in Figs. 1(a) and 1(b) reveal an excellent conformation of graphene sheet over the crests and the complete suspension in the region between them. In particular, the AFM profiles before and after deposition [solid and dashed lines in Fig. 1(b), respectively] indicate that graphene tends to mechanically relax to a configuration where a small fraction adheres to the sidewalls of the groove.

The graphene membrane was then characterized by Raman spectroscopy, a well-established method used to quantify the purity, thickness, and strain of graphene films

[36,38–40]. Figure 1(c) presents the typical Raman spectra obtained from analyzing both the supported graphene (black line) and suspended graphene (red line) of the deposited graphitic film. The shape of the two prominent  $G$  and  $2D$  peaks (both symmetric Lorentzian line shape, and width  $W_G = 12 \text{ cm}^{-1}$  and  $W_{2D} = 33 \text{ cm}^{-1}$ , respectively) indicates a high-quality, single-layer suspended graphene film [38–41]. The absence of the disorder-related  $D$  peak near  $1350 \text{ cm}^{-1}$  on the suspended part and the weak intensity on the supported one indicate that CVD graphene film is composed of large, defect-free single-crystal domains. The downward shift of both peaks positions in the suspended regions with respect to the supported graphene is evident and indicative of the different extent of both deformation and doping effects [38] in the two regions.

To disentangle doping and strain effects, we performed extensive Raman maps on graphene on the patterned area and graphene supported on the surrounding flat silicon region. Each map comprised about 80 points where we measured and fit Raman spectra to obtain  $G$  and  $2D$  peak positions (Pos $G$  and Pos $2D$  in the following). We computed the Pos $2D$ /Pos $G$  correlation shown in Fig. 1(d) following the protocol developed by Lee *et al.* [36]. Pos $G$  and Pos $2D$  are linearly correlated even within an ideal graphene sheet because of the ubiquitous presence of doping and strain effects. The slope of the linear distribution is indicative of the relative importance of either doping or strain effects. The solid blue lines in Fig. 1(d) represents the linear pure-strain axis with slope 2.2 and the pure-doping axis with slope 0.7, respectively [36]. The two axes cross at the neutrality point marked by a black dot at position ( $1581.6$  and  $2676.9 \text{ cm}^{-1}$ ) [36]. While on the doping line only positive values are physically meaningful, the convention adopted for strain evaluation is to indicate as a negative value the compressive strain that moves the peak towards higher frequencies and as a positive value the tensile strain inducing shift in the opposite direction [42]. The gray dot and the related gray line represent data from supported graphene while green and red data come from graphene over the patterned area. Data from supported graphene (gray symbols) indicate only a very slight tensile strain as well as a hole-doping effect, consistent with the literature for supported CVD graphene [39]. Raman spectra acquired from graphene within the pattern split into two sets with different slopes (green and red symbols). The green dots show a trend compatible with the reference signal (supported graphene) and, hence, they are attributed to the crest region, where graphene is supported. Indeed, the fitted slope [green and gray lines in Fig. 1(d)] is 0.94 in both cases, a value consistent with the literature [39]. By contrast, the red data are representative of suspended graphene: They group close to the doping axis so that the extrapolation towards strain axis indicates a negligible prestrain. Indeed, the linear fit yields a slope of 1.13 consistent with the value of 1.09 reported by Gajewski *et al.* [39] for suspended graphene. Hence, our sample presents no prestrain, probably because the portion of membrane adhering to the sidewall of the groove is small and its effect negligible.

### III. RESULTS AND DISCUSSION

Following the structural results of the Raman spectroscopy analysis, the membrane rheology was probed by friction force microscopy (FFM) (Fig. 2). FFM scans in two opposite directions were performed on a  $1\text{-}\mu\text{m}^2$  area, corresponding to the central region suspended between two crests [blue square in Fig. 2(a)]. By tilting the sample  $90^\circ$ , the same area was first scanned in the direction orthogonal to the groove axis and then in the one parallel to the groove axis, as indicated in the right side of Fig. 2(a) by black and red arrows, respectively. The same area was analyzed in both directions with positioning accuracy of the order of  $100 \text{ nm}$  ([43,44] and details in Supplemental Material [37]).

Care has been taken to analyze regions free from pre-existing extended wrinkles, which are clearly identifiable due to the strong contrast they produce on the lateral force signal [45]. On the contrary, ripple effects on graphene either of an intrinsic type or induced by tip or point defect [46] cannot be resolved since the induced elastic deformations during FFM measurements are larger with respect to ripple corrugation.

The measured frictional dissipation  $F$  was found to depend strongly on the scanning direction: The friction force recorded during scans parallel to the groove was typically three times that the orthogonal, at the same load  $P$  [see Fig. 2(b) and Fig. S2(a)]. The orthogonal vs parallel friction increase was then measured at different loads, from about  $25 \text{ nN}$  down to the negative pull-off force. Figure 2(b) reports the typical friction vs load behavior observed in several different spots on the membrane. The differential friction coefficient  $dF/dP$  (COF) was evaluated for each friction vs load curve and used as a representative parameter of the membrane anisotropic response. Figure 2(c) summarizes the statistics of our multispot analysis, revealing a remarkably consistent threefold increase from orthogonal to parallel scanning direction.

In particular, we notice that along the orthogonal direction the extremely low COF values are in agreement with those measured by Deng *et al.* on single-, bi-, and trilayer graphene suspended on micrometer-size circular hole [47] and confirmed recently by Zhan [27]. These values approach that of thick graphite [48], suggesting the absence of important elastic deformation effects. Comparison with graphene-supported systems is nontrivial since the specific tribological behavior depends on the substrate on which the graphene is deposited [27,49]. In general, the higher the adhesion towards the substrate the lower the out-of-plane deformation effect and the lower the friction coefficient [50,51]. Our results, summarized in Fig. 2(c), reveal that along the orthogonal direction the membrane behaves like a graphene layer with minor load-induced out-of-plane deformations, while along the parallel direction load-dependent deformation effects seem to become increasingly important.

The FFM scans were performed over hundreds of nanometers, providing the mesoscopic tribological response arising from a nanoscale contact. Over this length scale the atomistic stick-slip events cannot be detected by our equipment. Nevertheless, the atomistic nature of the dissipation can be

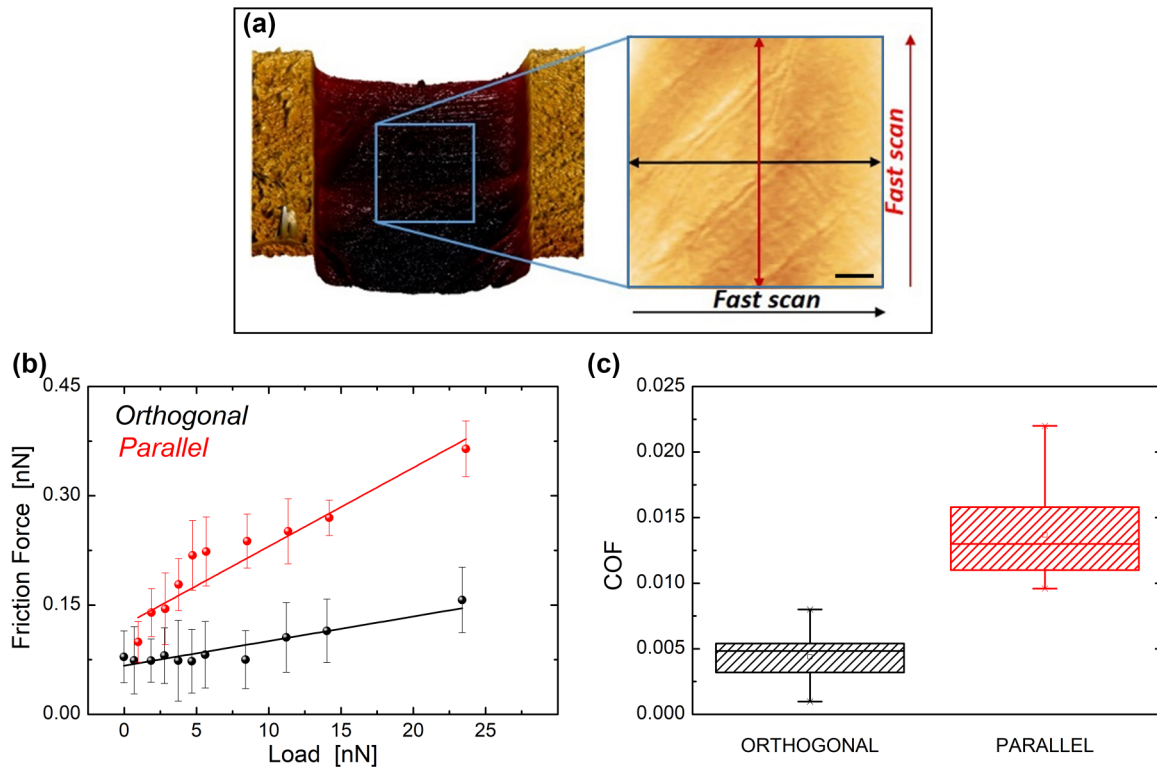


FIG. 2. Direction-dependent friction response of suspended CVD graphene. (a) Three-dimensional topography reconstruction of free-standing CVD graphene over single groove and 2D zoom of the region analyzed by FFM (blue square:  $1 \times 1 \mu\text{m}^2$ ); the two scan directions are represented with double-headed arrows (black for the orthogonal and red for the parallel, respectively). Scale bar corresponds to 150 nm. (b) Friction force as a function of load applied to free-standing CVD graphene with groove axis oriented orthogonal (black) and parallel (red) to the fast scan direction; circles represent experimental data with their error bars and continuous lines are the respective linear fit. (c) Boxplots of COF for orthogonal (black) and parallel (red) scans; counting corresponds to 12 different regions for orthogonal scans and to 19 for parallel scans, respectively.

indirectly assessed from the velocity dependency of the COF. We found that halving and doubling the sliding velocity yielded the same COF (Supplemental Material [37]). This velocity independence of friction in both directions is the fingerprint of the stick-slip regime, whereas a viscous dissipation would yield a linear dependence [52].

In order to understand the atomistic mechanism underlying the microscopic experimental measures, we consider the minimalistic model sketched in Fig. 3(a), which retains the experimental features assumed to be at the origin of the observed behavior. The stick-slip regime indicated by the experiments suggests that the fundamental dissipation mechanism should be captured by the Prandtl-Tomlinson (PT) model [53,54], allowing for the tip to be reduced to a point-like object [blue dot in Fig. 3(a)] sliding over a corrugated energy landscape. The cantilever was modeled as a mass moving at constant velocity  $v_{\text{drag}}$  [red square in Fig. 3(a)], dragging the tip via a spring of constant  $K$  (see Supplemental Material [37] and a benchmark of the model parameters at Refs. [27,55,56]).

Construction of the substrate in the PT model (i.e., the 2D membrane on which the tip slides) was key in this model, as it needed to capture the deformable nature of the suspended graphene sheet while at the same time preserving the atomistic nature of the contact—a smooth membrane cannot yield a stick-slip dynamics and a discrete graphene membrane

without the mesoscopic clamping asymmetry cannot deform realistically under the tip. To achieve a reasonable tradeoff between these two opposite requirements, we modeled the experimental membrane as a classical graphene sheet where the Adaptive intermolecular reactive empirical bond order (AIREBO) [56] potential describes intralayer interactions and Lennard-Jones (LJ) potential [27] interactions between the tip and graphene. To reproduce the asymmetric geometry, the membrane was finite in the  $x$  direction (orthogonal), and periodic in the  $y$  direction (parallel). To mimic the adhesion to the groove's crests, the membrane edges in the  $x$  direction were clamped with springs of constant  $Q = 1602 \text{ N/m}$  to the equilibrium position, marked by black straight line in Fig. 3(a). Hence, the simulated membrane was suspended and the clamping springs provided the restoring force opposing the one exerted by the tip upon loading and sliding. In Fig. 3(a) the clamped side is the zigzag edge while the periodic side is the armchair edge. Effects of finite size, edge orientation, and full open-boundary conditions are discussed in the Supplemental Material. The simulations were performed at zero temperature to obtain a clear signal and because the stick-slip dynamics is regulated by the energy barrier, while temperature introduces thermolubricity without qualitatively modifying the dynamics [53,54]. As the tip in experiments moved orders of magnitude slower than the relaxation time of the atomistic motion, a viscous damping was

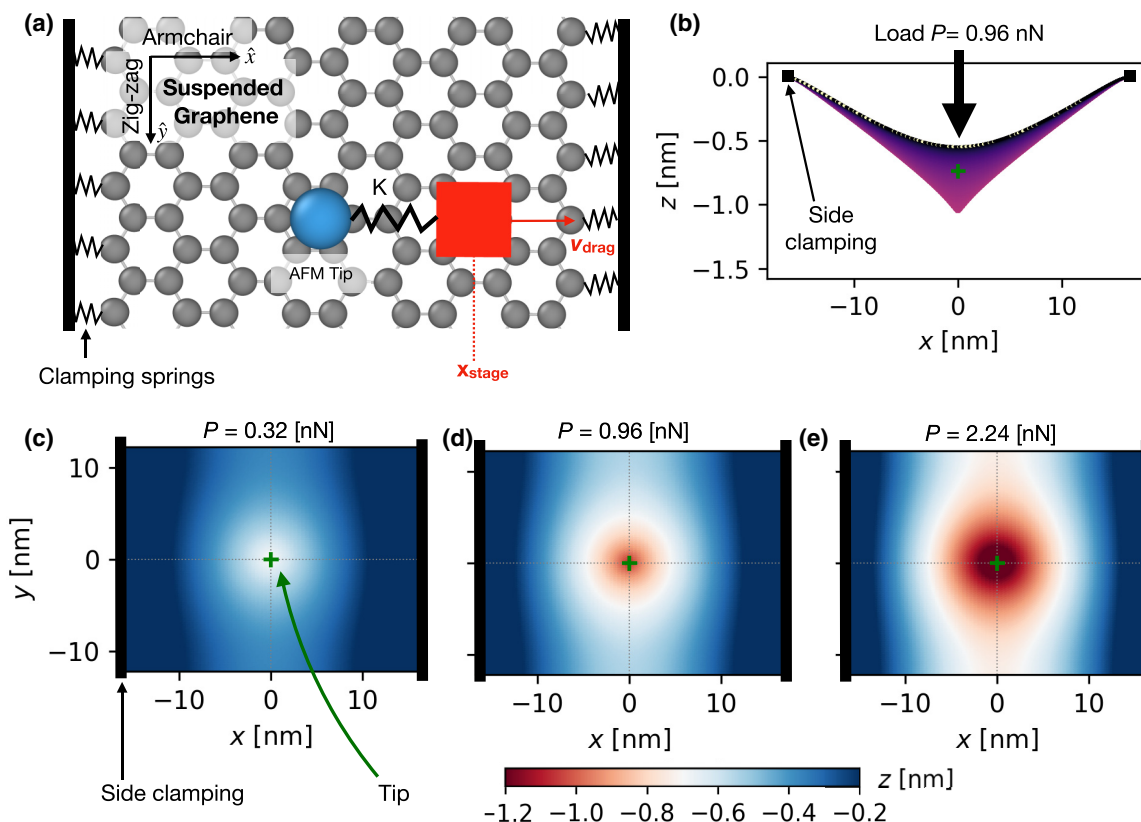


FIG. 3. (a) Model setup. Free-standing graphene membrane is clamped along the edges in the  $y$  direction at fixed  $x$  coordinate, consistently with experimental orientation in Fig. 1(a). Clamping is realized by attaching a stiff spring ( $Q = 1602 \text{ N/m}$ ) to each edge carbon atom in a  $0.25\text{-nm}$  region. As reported in the top left corner, the zigzag edge is clamped while the armchair one is free (see Supplemental Material for results with the opposite orientation, namely clamped armchair and free zigzag). Prandtl-Tomlinson tip (blue sphere) indents the membrane under a constant vertical load (along  $z$ ). Mimicking a minimal AFM setup, the tip is attached to a moving stage (red cube), representing the massive cantilever, translating at constant velocity  $v_{\text{drag}}$ . Side- (b) and top (c)–(e) views of the indentation profile. Purple region in (b) reports the position projected on  $x$  and the black squares indicate the position of the clamps. Note that the axes in (b) are not in scale, i.e., the deformation of the membrane is accentuated for visual aid. (c)–(e) Top view of the indentation profile for increasing loads, as reported at the top of each plot: The tip (green cross) indents the center of the membrane and the system is relaxed (see Supplemental Material for the relaxation protocol). Color scale in (c)–(e) reports the vertical deformation of the membrane, as indicated by the color bar at the bottom. Black bar at the sides indicates the position of the clamps, as in (a). Gray dashed lines in (c)–(e) mark the reference  $x = 0$ ,  $y = 0$ , as a guide to the eye. Height of each C atom of the membrane has been linearly interpolated on a finer grid for clearer visualization.

applied to all the atoms. The crucial property we rely upon is the near independence of stick-slip friction upon velocity [52].

An external load  $P$  was applied to the model tip [as sketched in Fig. 3(b)], which indents the membrane, as shown in Figs. 3(c)–3(e) for increasing loads. The indentation shape follows the asymmetric geometry. The deformation is radial under the tip [green cross in Figs. 3(c)–3(e)], but this symmetry is lost far away from it, in particular nearing the edges: The membrane forms an elongated “valley” in the parallel direction [white regions in Figs. 3(c)–3(e)] and remains almost flat near the clamps [blue regions in Figs. 3(c)–3(e)]. This characteristic indentation shape becomes more evident as the load increases, as shown in going from Fig. 3(c) to Fig. 3(e).

For each indentation load, the tip can slide in the orthogonal and parallel directions. The sliding was performed for a load from 0 to  $2.24 \text{ nN}$ . Note that the loads applied to a point-like tip do not relate directly to the experimental one. One can estimate the relative pressure and membrane vs tip-size ratio between MD and experiments. Taking the equilibrium

tip-membrane distance according to the LJ potential  $R = 0.35 \text{ nm}$  as tip radius in MD and assuming a Hertzian contact area (see Supplemental Material [37] and Refs. [57,58]), at the maximum load  $P = 2.2 \text{ nN}$  the pressure was  $12.8 \text{ GPa}$ , much higher than experiments where the maximum estimated pressure was  $28 \text{ MPa}$  at load  $20 \text{ nN}$ . At the same time, in the experiments the load was applied on an extended tip of radius  $R = 15 \text{ nm}$ , while the real contact area of the single asperity undergoing stick-slip is certainly smaller (and thus pressure is higher) but difficult to estimate [59]. A more meaningful quantity to compare between simulations and experiments is the ratio between the tip radius  $R$  and the membrane clamped length  $L$ . This ratio is  $R/L = 0.011$  in simulations and  $R/L = 0.01$  in experiments, with a groove distance  $L = 1.5 \mu\text{m}$ . The two values are comparatively close, suggesting that while the nominal pressure in the MD simulations is higher than the experimental one, the dimensional ratio is correctly described by the model. This geometrical element is crucial to address the anisotropy

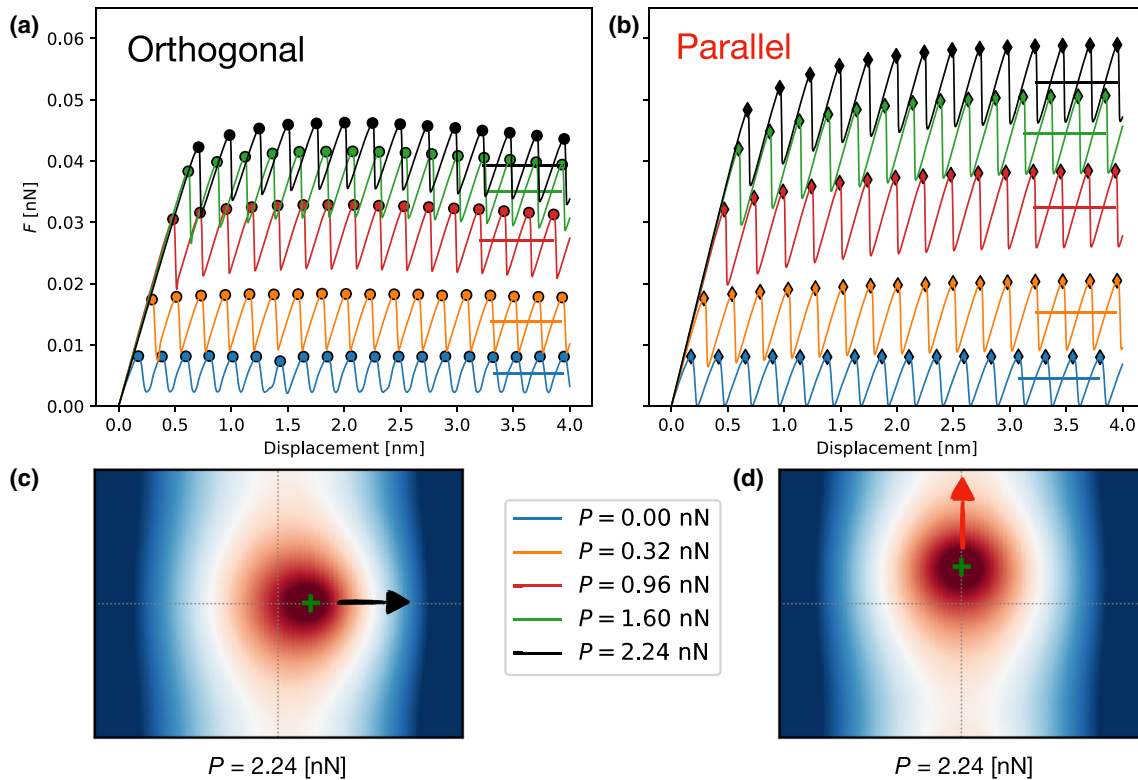


FIG. 4. Simulated frictional response of the membrane perpendicular (a) and parallel (b) to the clamps. The y axis reports the force on the cantilever while  $x$  reports the cantilever position. Each colored line corresponds to a load, as reported in the legend in the bottom right. The friction traces are normalized by the elastic charging of the membrane as reported in Supplemental Material. Color-matching horizontal lines show the average friction force at each load after the initial transient. Note that the average excludes the end of the simulation to limit the influence of the clamps in (a) and of the free edge in (b). Panels (c), (d) show the tip-sliding direction and the evolution from the indentation profile in Fig. 3(e) toward the end of the trajectory; color scale is the same as Fig. 3. Dashed horizontal and vertical gray lines indicate  $x = 0$  and  $y = 0$  as a guide to the eye.

observed in experiments because the size relationship between the indenter and the intended membrane sets the shape of the indentation pattern and the strain distribution.

Force traces along the orthogonal and parallel directions for selected loads are reported in Figs. 4(a) and 4(b), respectively. The atomistic stick-slip behavior is evident at all loads, owing to the damped, zero-temperature dynamics of the MD simulations. As the cantilever started to translate, the tip climbed the corrugation energy barrier; see the initial increase of all lines in Figs. 4(a) and 4(b). Once the cantilever restoring force overpowered the barrier, the system depinned, causing the first drop in all lines in Figs. 4(a) and 4(b). This is the onset of static friction. Afterwards, the tip moved by single-lattice slips, yielding the characteristic sawtooth force profile of stick-slip dynamics shown in Figs. 4(a) and 4(b). As shown in detail in Supplemental Material [37], the membrane deformation instantaneously follows the tip motion: There is an adiabatic separation between slow motion of the AFM tip and the fast relaxation of the membrane, as in experiments.

After an initial transient, the kinetic friction was calculated as the average sliding force shown in Figs. 4(a) and 4(b) as horizontal lines. The protocol to compute kinetic friction in this clamped system is described in detail in the Supplemental Material [37].

From Figs. 4(a) and 4(b) one can already see that the friction in the orthogonal direction is smaller than in the parallel one, as in experimental curves in Fig. 2(b). The force-load curves for the two directions are obtained by plotting the average friction force, horizontal lines in Figs. 4(a) and 4(b), against the applied load  $P$ . Figure 5(a) reports the average friction vs load for the orthogonal (blue line) and parallel (orange line). For small loads ( $P = 0-0.5$  nN), where the anisotropic mechanical constraint of the clamping is very modestly perceived, the two curves behave similarly; as the load increases, however, the average force in the parallel direction keeps rising, while in the orthogonal direction the growth slows down. This follows the experimental behavior in Fig. 2(b), where parallel force is higher while perpendicular is smaller. Even though the model force-load curves in Fig. 5(a) showed a clear nonlinear trend, as reasonable for the system, the concept of differential COF helps to establish a systematic comparison with experiment. Considering only the large-load limit [dashed lines in Fig. 4(a)], we obtained  $COF_{\perp} = 0.013$  and  $COF_{\parallel} = 0.023$ , yielding a ratio  $COF_{\parallel}/COF_{\perp} = 1.7$ . We conclude that this minimal model is able to reproduce fairly well the experimental finding  $COF_{\parallel} \gg COF_{\perp}$ .

Note that the COFs from MD simulations are higher than in experiments. This discrepancy can be linked to the system being an ideal crystal at zero temperature, representing an

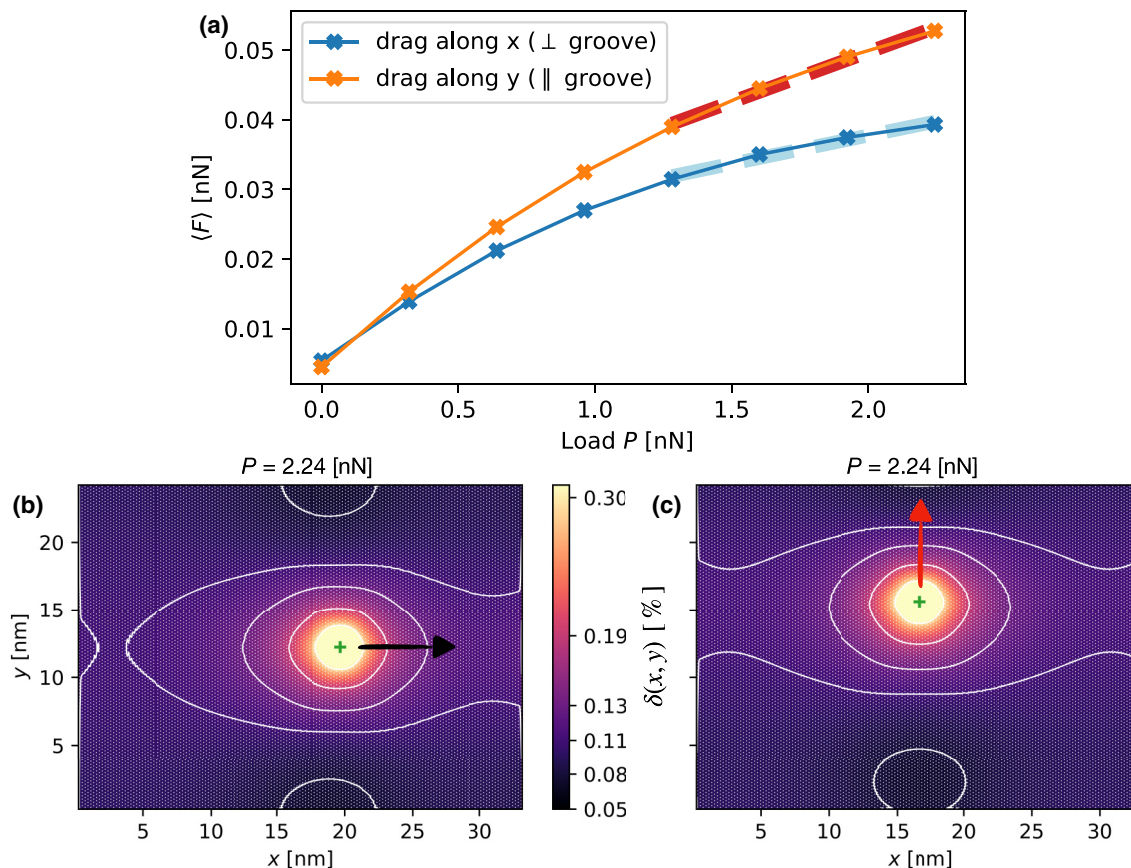


FIG. 5. (a) Average friction vs load for the direction perpendicular (blue curve) and parallel (orange) to the clamp. COF perpendicular and parallel to the clamps is defined as the slope of the light-blue and red-dashed lines, respectively. (b), (c) Overall strain of each carbon atom as bond-length difference averaged over its nearest neighbors. (b) Final snapshot of orthogonal dragging, and (c) for parallel dragging; both snapshots refer to load  $P = 2.24$  nN [black curves in Figs. 4(a) and 4(b) and last point in (a)]. Green cross marks the tip position. Darker regions mark smaller strain, lighter regions higher strain. White lines mark the isoline at the values reported on the color bar.

upper bound for the friction force in the real system. At the same, the agreement between trends found in experiments and in MD simulations are robust against variations of crystal orientation and boundary conditions (see Supplemental Material [37] and Ref. [60]). Hence, we believe the physics underpinning the experimental results are well described by the theoretical model, while the assumptions of the model result in a qualitative rather than quantitative agreement.

These “*in silico* frictional experiments” were crucial to understand the origin of this asymmetric rheological response of suspended graphene in absence of prestrain. Figures 5(b) and 5(c) report the model strain distribution in the membrane as the bond-length deviation from equilibrium,  $\langle \delta \rangle_{nm} = \langle \frac{l-l_0}{l_0} \rangle_{nm}$ , where  $l_0 = 0.139$  nm is the equilibrium C–C bond length in MD and the  $\langle \cdot \rangle_{nm}$  indicates the average over the nearest neighbors of each carbon atom. While no prestrain is present in the membrane, the tip indentation stretches the membrane up to  $\delta \sim 2\%$  right below the tip as shown by the large yellow patch in Figs. 5(b) and 5(c). This tip-induced strain is larger in the orthogonal direction, as the graphene needs to comply with both the tip pressure and the clamps pull [see the brighter horizontal strip highlighted by the white contour lines in Fig. 5(b)]. Hence, the membrane is stiffer in the transverse direction. On the other hand, in the parallel direction the tip-induced strain is lower [see the black regions enclosed by the

white contour lines in Fig. 5(c)]. When the tip was dragged along the transverse direction, the stiff substrate was not deformed significantly by the pushing tip and the force needed to slide was small. Conversely, when the tip was driven along the parallel direction the graphene membrane deformed easily under the action of the sliding probe, resulting in a higher force opposing sliding and, thus, a higher dissipation. As the load increases, the orthogonal direction becomes stiffer, enhancing this effect and leading to the smaller coefficient of friction shown in Fig. 5(a).

The computational results indicate that the anisotropic stiffening of the membrane induced by the clamping during indentation, and not an anisotropic prestrain, which is absent in our case, is the mechanism underpinning the different frictional response in the orthogonal and parallel directions. This argument is further corroborated by the experiments. Analyzing the effective piezoeelongation as a function of the applied loads during the acquisition of friction vs load images (see Supplemental Material [37]), we can extract the tip-induced elastic deformations of graphene along both the orthogonal and parallel directions of the groove. This analysis provided an estimate of the effective elastic constant ( $K_{\text{eff}}$ ) for the coupled graphene-cantilever system. The mechanics is that of two springs in series: One is given by the flexural constant  $K_N$  of the AFM cantilever; the other represents the elastic

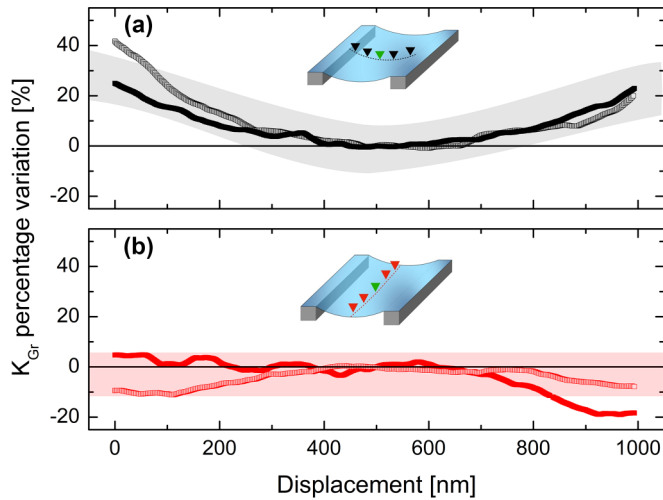


FIG. 6. Elastic behavior of the graphene membrane along the orthogonal (black) and parallel (red) scan directions (light and dark lines correspond to different membranes). Elastic constant of the graphene membrane is evaluated as discussed in text and in Supplemental Material [37]. Data are normalized to the values evaluated at the membrane center (green triangle in the insets) and they are shown as relative percentage variation. In the orthogonal direction the relative variation of  $K_{Gr}$  near the clamping regions achieves 40% while along the parallel direction it is almost always contained within 10%. Reference values at the center are membrane 1 (dark line)  $K_{Gr} = 0.455 \pm 0.05$  (N/m); and membrane 2 (light line)  $K_{Gr} = 0.46 \pm 0.15$  (N/m).

response of the graphene membrane subject to normal load, whose constant is termed here  $K_{Gr}$ .

Figure 6 reports the variation of the graphene elasticity  $K_{Gr}$  as a function of the positions along the orthogonal [Fig. 6(a)] and parallel direction [Fig. 6(b)] with respect to the value at the center of the path. In the orthogonal direction, the relative variation of  $K_{Gr}$  near the clamping regions achieves 40%, while along the parallel direction the variation is almost negligible (within 10% of the value at the center).

Hence, the intrinsic membrane elasticity as described by  $K_{Gr}$  strongly depends on the scan direction. In particular, the orthogonal scan reveals a nonuniform response along the profile: The center region is softer while the system gradually becomes effectively stiffer approaching the clamping constraints. On the contrary, in the parallel scan direction, the response is essentially constant, as expected from the model. The behavior described by the intrinsic membrane elasticity is consistent with computational results: The induced strain reported in Figs. 5(b) and 5(c) indicates anisotropic membrane stiffness along the two sliding directions. Tip sliding along the orthogonal direction [Fig. 5(b)] moved toward higher strain regions near the clamps compared to the center: The membrane became stiffer. Conversely, when the tip slid along

the parallel direction [Fig. 5(c)] the strain distribution just translated unchanged with the tip, yielding the same stiffness along the path.

#### IV. CONCLUSIONS

The effect of in-plane strain on the frictional mechanics of free-standing 2D membranes has been addressed only recently. Within the effort of understanding the nanorheology of 2D materials under strain, graphene has been investigated in different conformations, from freely suspended on a circular hole to strained as the hole gets pressurized. We found unexpected results on the asymmetric tribological response of a single-layer CVD graphene freely suspended over a specially designed groove geometry. FFM measurements and friction vs load analysis performed at the membrane center reveal a remarkably large anisotropy with respect to the groove axis. A very low COF is measured by sliding transverse to the groove while an unexpected nearly threefold increase is obtained when moving parallel. As the prestrain discussed in the literature is absent in our system, a different mechanism is required to explain the observed anisotropy. Our MD model, corroborated by subsequent measurements, suggests that deformation induced by indenting and sliding action of the tip is anisotropic due to the asymmetric clamping conditions. This also reflects in anisotropic friction response of the graphene membrane. Sliding orthogonally to grooves produces a larger strain, where the membrane stiffens and the force needed to drive the tip drops. On the contrary, moving parallel to grooves the graphene membrane deforms easily and a larger force is needed to slide. This mechanism is amplified with increasing load, which results in an asymmetric dependence of friction vs load.

These experimental results complemented by numerical simulations demonstrate how strong adhesion (clamping) and decoupling (suspension) from the substrate can modulate the stiffness and the friction on these membranelike systems. Strongly anisotropic geometries, such as that investigated here, are likely to occur in realistic systems. Hence, we believe that our results and analysis will be relevant to design and tune future graphene-based systems such as nanomechanical devices and ultralow-friction coatings.

#### ACKNOWLEDGMENTS

A.M., G.P., A.S., and A.V. acknowledge support by the Italian Ministry of University and Research through PRIN UTFROM Grant No. 20178PZCB5. E.T. acknowledges support by ERC ULTRADISS Contract No. 834402.

G.P. and A.M. conceptualized the experimental work and performed the experiments; A.S. and A.K. performed the simulations; A.S., A.V., and E.T. conceptualized the simulations; all authors analyzed the data and wrote the manuscript.

[1] R. J. Young, I. A. Kinloch, L. Gong, and K. S. Novoselov, The mechanics of graphene nanocomposites: A review, *Compos. Sci. Technol.* **72**, 1459 (2012).

[2] Q. Cao, X. Geng, H. Wang, P. Wang, A. Liu, Y. Lan, and Q. Peng, A review of current development of graphene mechanics, *crystals* **8**, 357 (2018).



- [3] S. Luo, Y. A. Samad, V. Chan, and K. Liao, Cellular graphene: Fabrication, mechanical properties, and strain-sensing applications, *Matter* **1**, 1148 (2019).
- [4] C. Galiotis, O. Frank, E. N. Koukaras, and D. Sfyris, Graphene mechanics: Current status and perspectives, *Annu. Rev. Chem. Biomol. Eng.* **6**, 121 (2015).
- [5] C. Lee, X. Wei, J. W. Kysar, J. Hone, and J. Marrow, Measurement of the elastic properties and intrinsic strength of monolayer graphene, *Science* **321**, 385 (2008).
- [6] Y. Gao, S. Kim, C. H.-C., D. Nélias, C. Berger, W. de Heer, L. Polloni, R. Sordan, A. Bongiorno, and E. Riedo, Elastic coupling between layers in two-dimensional materials, *Nat. Mater.* **14**, 714 (2015).
- [7] U. Ludacka, M. R. A. Monazam, C. Rentenberger, M. Friedrich, U. Stefanelli, J. C. Meyer, and J. Kotakoski, In situ control of graphene ripples and strain in the electron microscope, *npj 2D Mater. Appl.* **2**, 25 (2018).
- [8] I. V. Gornyi, V. Y. Kachorovskii, and A. D. Mirlin, Anomalous Hooke's law in disordered graphene, *2D Mater.* **4**, 011003 (2016).
- [9] K. Cao, S. Feng, Y. Han, L. Gao, T. Hue Ly, Z. Xu, and Y. Lu, Elastic straining of free-standing monolayer graphene, *Nat. Commun.* **11**, 284 (2020).
- [10] V.-M. Hiltunen, P. Koskinen, K. K. Mentel, J. Manninen, P. Myllyperkiö, M. Pettersson, and A. Johansson, Ultrastiff graphene, *npj 2D Mater. Appl.* **5**, 49 (2021).
- [11] K. S. Novoselov, V. I. Fal'ko, L. Colombo, P. R. Gellert, M. G. Schwab, and K. Kim, A roadmap for graphene, *Nature (London)* **490**, 192 (2012).
- [12] Y. Shao, M. F. El-Kady, L. J. Wang, Q. Zhang, Y. Li, H. Wang, M. F. Mousavi, and R. B. Kaner, Graphene-based materials for flexible supercapacitors, *Chem. Soc. Rev.* **44**, 3639 (2015).
- [13] A. Mehmood, N. M. Mubarak, M. Khalid, R. Walvekar, E. C. Abdullah, M. T. H. Siddiqui, H. A. Baloch, S. Nizamuddin, and S. Mazari, Graphene based nanomaterials for strain sensor application—a review, *J. Environ. Chem. Eng.* **8**, 103743 (2020).
- [14] R. J. Dolleman, D. Davidovikj, S. J. Cartamil-Bueno, H. S. J. van der Zant, and P. G. Steeneken, Graphene squeeze-film pressure sensors, *Nano Lett.* **16**, 568 (2016).
- [15] Z. Yang, Y. Pang, X. Han, Y. Yang, J. Ling, M. Jian, Y. Zhang, Y. Yang, and T.-L. Ren, Graphene textile strain sensor with negative resistance variation for human motion detection, *ACS Nano* **12**, 9134 (2018).
- [16] M. Liu, Z. Li, X. Zhao, R. J. Young, and I. A. Kinloch, Fundamental insights into graphene strain sensing, *Nano Lett.* **21**, 833 (2021).
- [17] X. Zhao, B. Mao, M. Liu, J. Cao, S. J. Haigh, D. G. Papageorgiou, Z. Li, and R. J. Young, Controlling and monitoring crack propagation in monolayer graphene single crystals, *Adv. Funct. Mater.* **32**, 2202373 (2022).
- [18] C. Liu, B. Yao, T. Dong, H. Ma, S. Zhang, J. Wang, J. Xu, Y. Shi, K. Chen, L. Gao, and L. Yu, Highly stretchable graphene nanoribbon springs by programmable nanowire lithography, *npj 2D Mater. Appl.* **3**, 23 (2019).
- [19] D. Kireev, S. K. Ameri, A. Nederveld, J. Kampfe, H. Jang, N. Lu, and D. Akinwande, Fabrication, characterization and applications of graphene electronic tattoos, *Nat. Protoc.* **16**, 2395 (2021).
- [20] D. Kireev, J. Kampfe, A. Hall, and D. Akinwande, Graphene electronic tattoos 2.0 with enhanced performance, breathability and robustness, *npj 2D Mater. Appl.* **6**, 46 (2022).
- [21] X. Fan, A. D. Smith, F. Forsberg, S. Wagner, S. Schröder, S. S. A. Akbari, A. C. Fisher, L. G. Villanueva, M. Östling, M. C. Lemme, and F. Niklaus, Manufacture and characterization of graphene membranes with suspended silicon proof masses for MEMS and NEMS applications, *Microsyst. Nanoeng.* **6**, 17 (2020).
- [22] F. M. D. Pellegrino, G. G. N. Angilella, and R. Pucci, Strain effect on the optical conductivity of graphene, *Phys. Rev. B* **81**, 035411 (2010).
- [23] X. He, L. Gao, N. Tang, J. Duan, F. Xu, X. Wang, X. Yang, W. Ge, and B. Shen, Shear strain induced modulation to the transport properties of graphene, *Appl. Phys. Lett.* **105**, 083108 (2014).
- [24] H. Zhang, J.-W. Huang, J. Velasco, Jr., K. Myhro, M. Maldonado, D. Dung Tran, Z. Zhao, F. Wang, Y. Lee, G. Liu, W. Bao, and C. Ning Lau, Transport in suspended monolayer and bilayer graphene under strain: A new platform for material studies, *Carbon* **69**, 336 (2014).
- [25] R. Schmidt, I. Niehues, R. Schneider, M. Drüppel, T. Deilmann, M. Rohlfing, S. M. de Vasconcellos, A. Castellanos-Gomez, and R. Bratschitsch, Reversible uniaxial strain tuning in atomically thin  $\text{WSe}_2$ , *2D Mater.* **3**, 021011 (2016).
- [26] F. Wang, S. Li, M. A. Bissett, I. A. Kinloch, Z. Li, and R. J. Young, Strain engineering in monolayer  $\text{WS}_2$  and  $\text{WS}_2$  nanocomposites, *2D Mater.* **7**, 045022 (2020).
- [27] S. Zhang, Y. Hou, S. Li, L. Liu, Z. Zhang, X.-Q. Feng, and Q. Li, Tuning friction to a superlubric state via in-plane straining, *Proc. Natl. Acad. Sci. USA* **116**, 24452 (2019).
- [28] K. Wang, C. Qu, J. Wang, W. Ouyang, M. Ma, and Q. Zheng, Strain engineering modulates graphene interlayer friction by moiré pattern evolution, *ACS Appl. Mater. Interfaces* **11**, 36169 (2019).
- [29] C. Xu, S. Zhang, H. Du, T. Xue, Y. Kang, Y. Zhang, P. Zhao, and Q. Li, Revisiting frictional characteristics of graphene: Effect of in-plane straining, *ACS Appl. Mater. Interfaces* **14**, 41571 (2022).
- [30] C. Lee, Q. Li, W. Kalb, X.-Z. Liu, H. Berger, R. W. Carpick, and J. Hone, Frictional characteristics of atomically thin sheets, *Science* **328**, 76 (2010).
- [31] P. Egberts, G. H. Han, X. Z. Liu, A. T. C. Johnson, and R. W. Carpick, Frictional behavior of atomically thin sheets: Hexagonal-shaped graphene islands grown on copper by chemical vapor deposition, *ACS Nano* **8**, 5010 (2014).
- [32] G. Paolicelli, M. Tripathi, V. Corradini, A. Candini, and S. Valeri, Nanoscale frictional behavior of graphene on  $\text{SiO}_2$  and Ni(111) substrates, *Nanotechnology* **26**, 055703 (2015).
- [33] X. Wang, K. Tantiwanichapan, J. W. Christopher, R. Paiella, and A. K. Swan, Uniaxial strain redistribution in corrugated graphene: Clamping, sliding, friction, and 2D band splitting, *Nano Lett.* **15**, 5969 (2015).
- [34] A. Mescola, G. Paolicelli, S. P. Ogilvie, R. Guarino, J. G. McHugh, A. Rota, E. Iacob, E. Gnecco, S. Valeri, N. M. Pugno, V. Gadhamshetty, M. M. Rahman, P. Ajayan, A. B. Dalton, and M. Tripathi, Graphene confers ultralow friction on nanogear cogs, *Small* **17**, 2104487 (2021).

- [35] T. Rakib, P. Pochet, E. Ertekin, and H. T. Johnson, Corrugation-driven symmetry breaking in magic-angle twisted bilayer graphene, *Commun. Phys.* **5**, 242 (2022).
- [36] J. E. Lee, G. Ahn, J. Shim, Y. S. Lee, and S. Ryu, Optical separation of mechanical strain from charge doping in graphene, *Nat. Commun.* **3**, 1024 (2012).
- [37] See Supplemental Material at <http://link.aps.org/supplemental/10.1103/PhysRevMaterials.7.054007> for sample preparation (Fig. S1) and characterization by Raman analysis; AFM and FFM procedure; sliding regime/friction profiles and COF-velocity independency (Fig. S2); elastic deformation of the membrane (Figs. S3 and S4); MD simulations, in particular, method, finite-size effect (Fig. S5), force friction protocol (Fig. S6), force friction armchair OBC (Figs. S7, S8, and S9). The Supplemental Material also contains Refs. [27,43,44,55–58,60].
- [38] A. C. Ferrari, J. C. Meyer, V. Scardaci, C. Casiraghi, M. Lazzeri, F. Mauri, S. Piscanec, D. Jiang, K. S. Novoselov, S. Roth, and A. K. Geim, Raman Spectrum of Graphene and Graphene Layers, *Phys. Rev. Lett.* **97**, 187401 (2006).
- [39] K. Gajewski, S. Goniszewski, A. Szumska, M. Moczala, P. Kunicki, J. Gallop, N. Klein, L. Hao, and T. Gotszalk, Raman spectroscopy and Kelvin probe force microscopy characteristics of the CVD suspended graphene, *Diamond Relat. Mater.* **64**, 27 (2016).
- [40] J.-B. Wu, M.-L. Lin, X. Cong, H.-N. Liu, and P.-H. Tan, Raman spectroscopy of graphene-based materials and its applications in related devices, *Chem. Soc. Rev.* **47**, 1822 (2018).
- [41] S. Berciaud, S. Ryu, L. E. Brus, and T. F. Heinz, Probing the intrinsic properties of exfoliated graphene: Raman spectroscopy of free-standing monolayers, *Nano Lett.* **9**, 346 (2009).
- [42] J. Zabel, R. R. Nair, A. Ott, T. Georgiou, A. K. Geim, K. S. Novoselov, and C. Casiraghi, Raman spectroscopy of graphene and bilayer under biaxial strain: Bubbles and balloons, *Nano Lett.* **12**, 617 (2012).
- [43] J. E. Sader, J. W. M. Chon, and P. Mulvaney, Calibration of rectangular atomic force microscope cantilevers, *Rev. Sci. Instrum.* **70**, 3967 (1999).
- [44] C. P. Green, H. Lioe, J. P. Cleveland, R. Proksch, P. Mulvaney, and J. E. Sader, Normal and torsional spring constants of atomic force microscope cantilevers, *Rev. Sci. Instrum.* **75**, 1988 (2004).
- [45] M. Tripathi, F. Awaja, R. A. Bizard, S. Signetti, E. Iacob, G. Paolicelli, S. Valeri, A. Dalton, and N. M. Pugno, Friction and adhesion of different structural defects of graphene, *ACS Appl. Mater. Interfaces* **10**, 44614 (2018).
- [46] A. Zambudio, E. Gnecco, J. Colchero, R. Pérez, J. Gómez-Herrero, and C. Gómez-Navarro, Fine defect engineering of graphene friction, *Carbon* **182**, 735 (2021).
- [47] Z. Deng, N. N. Klimov, S. D. Solares, T. Li, H. Xu, and R. J. Cannara, Nanoscale interfacial friction and adhesion on supported versus suspended monolayer and multilayer graphene, *Langmuir* **29**, 235 (2013).
- [48] U. D. Schwarz, O. Zwörner, P. Köster, and R. Wiesendanger, Quantitative analysis of the frictional properties of solid materials at low loads. I. Carbon compounds, *Phys. Rev. B* **56**, 6987 (1997).
- [49] N. Manini, G. Mistura, G. Paolicelli, E. Tosatti, and A. Vanossi, Current trends in the physics of nanoscale friction, *Adv. Phys.:* **X 2**, 569 (2017).
- [50] T. Filleter, J. L. McChesney, A. Bostwick, E. Rotenberg, K. V. Emtsev, Th. Seyller, K. Horn, and R. Bennewitz, Friction and Dissipation in Epitaxial Graphene Films, *Phys. Rev. Lett.* **102**, 086102 (2009).
- [51] C. Xu, Z. Ye, and P. Egberts, Friction hysteretic behavior of supported atomically thin nanofilms, *npj 2D Mater. Appl.* **7**, 1 (2023).
- [52] A. Vanossi, N. Manini, M. Urbakh, S. Zapperi, and E. Tosatti, Colloquium: Modeling friction: From nanoscale to mesoscale, *Rev. Mod. Phys.* **85**, 529 (2013).
- [53] M. H. Müser, M. Urbakh, and M. O. Robbins, Statistical Mechanics of Static and Low-Velocity Kinetic Friction, in *Advances in Chemical Physics*, edited by I. Prigogine, and S. A. Rice (John Wiley & Sons, Inc., Hoboken, NJ, 2003), pp. 187–272.
- [54] A. Vanossi and O. M. Braun, Driven dynamics of simplified tribological models, *J. Phys.: Condens. Matter* **19**, 305017 (2007).
- [55] S. Plimpton, Fast parallel algorithms for short-range molecular dynamics, *J. Comput. Phys.* **117**, 1 (1995).
- [56] D. W. Brenner, O. A. Shenderova, J. A. Harrison, S. J. Stuart, B. Ni, and S. B. Sinnott, A second-generation reactive empirical bond order (REBO) potential energy expression for hydrocarbons, *J. Phys.: Condens. Matter* **14**, 783 (2002).
- [57] M. de Jong, W. Chen, T. Angsten, A. Jain, R. Notestine, A. Gamst, M. Sluiter, C. K. Ande, S. van der Zwaag, J. J. Plata, C. Toher, S. Curtarolo, G. Ceder, K. A. Persson, and M. Asta, Charting the complete elastic properties of inorganic crystalline compounds, *Sci. Data* **2**, 150009 (2015).
- [58] A. Jain, S. P. Ong, G. Hautier, W. Chen, W. D. Richards, S. Dacek, S. Cholia, D. Gunter, D. Skinner, G. Ceder, and K. A. Persson, Commentary: The materials project: A materials genome approach to accelerating materials innovation, *APL Mater.* **1**, 011002 (2013).
- [59] Y. Mo, K. T. Turner, and I. Szlufarska, Friction laws at the nanoscale, *Nature (London)* **457**, 1116 (2009).
- [60] C. M. Almeida, R. Prioli, B. Fagnéaud, L. G. Caçado, R. Paupitz, D. S. Galvão, M. De Cicco, M. G. Menezes, C. A. Achete, and R. B. Capaz, Giant and tunable anisotropy of nanoscale friction in graphene, *Sci. Rep.* **6**, 31569 (2016).